

Topological transmission and topological corner states combiner in all-dielectric honeycomb valley photonic crystals

Ming Sun(孙铭), Xiao-Fang Xu(许孝芳), Yun-Feng Shen(沈云峰), Ya-Qing Chang(常雅箐), and Wen-Ji Zhou(周文佶)

Citation: Chin. Phys. B, 2025, 34 (**3**): 034206. DOI: 10.1088/1674-1056/ada9d9
Journal homepage: http://cpb.iphy.ac.cn; http://iopscience.iop.org/cpb

What follows is a list of articles you may be interested in

Topological edge and corner states of valley photonic crystals with zipper-like boundary conditions

Yun-Feng Shen(沈云峰), Xiao-Fang Xu(许孝芳), Ming Sun(孙铭), Wen-Ji Zhou(周文佶), and Ya-Jing Chang(常雅箐)
Chin. Phys. B, 2024, 33 (**4**): 044203. DOI: 10.1088/1674-1056/ad1e6a

Topological states switching and group velocity control in two-dimensional non-reciprocal Hermitian photonic lattice

Yu Lin(林宇), Yuandan Wang(王元旦), Junhao Yang(杨俊豪), Yixuan Fu(符艺萱), and Xinyuan Qi(齐新元)
Chin. Phys. B, 2023, 32 (**11**): 114213. DOI: 10.1088/1674-1056/ad0621

Topological resonators based on hexagonal-star valley photonic crystals

Xin Wan(万鑫), Chenyang Peng(彭晨阳), Gang Li(李港), Junhao Yang(杨俊豪), and Xinyuan Qi(齐新元)
Chin. Phys. B, 2023, 32 (**11**): 114208. DOI: 10.1088/1674-1056/acf44b

High-performance chiral all-optical OR logic gate based on topological edge states of valley photonic crystal

Xiaorong Wang(王晓蓉), Hongming Fei(费宏明), Han Lin(林瀚), Min Wu(武敏), Lijuan Kang(康丽娟), Mingda Zhang(张明达), Xin Liu(刘欣), Yibiao Yang(杨毅彪), and Liantuan Xiao(肖连团)
Chin. Phys. B, 2023, 32 (**7**): 074205. DOI: 10.1088/1674-1056/accb41

Topological phases and type-II edge state in two-leg-coupled Su-Schrieffer-Heeger chains

Tianqi Luo(罗天琦), Xin Guan(关欣), Jingtao Fan(樊景涛), Gang Chen(陈刚), and Suo-Tang Jia(贾锁堂)
Chin. Phys. B, 2022, 31 (**1**): 014208. DOI: 10.1088/1674-1056/ac3650

Topological transmission and topological corner states combiner in all-dielectric honeycomb valley photonic crystals

Ming Sun(孙铭)[1], Xiao-Fang Xu(许孝芳)[1,2,†], Yun-Feng Shen(沈云峰)[1], Ya-Qing Chang(常雅箐)[1], and Wen-Ji Zhou(周文佶)[1]

[1] *School of Mechanical Engineering, Jiangsu University, Zhenjiang* 212003, *China*
[2] *School of Optical and Electronic Information, Suzhou City University & Suzhou Key Laboratory of Biophotonics, Suzhou* 215104, *China*

(Received 30 October 2024; revised manuscript received 1 January 2025; accepted manuscript online 14 January 2025)

We study the topological states (TSs) of all-dielectric honeycomb valley photonic crystals (VPCs). Breaking the space inversion symmetry of the honeycomb lattice by varying the filling ratio of materials for circular ring dielectric columns in the unit cell, which triggers topological phase transitions and thus achieves topological edge states (TESs) and topological corner states (TCSs). The results demonstrate that this structure has efficient photon transmission characteristics and anti-scattering robustness. In particular, we have found that changing the type of edge splicing between VPCs with different topological properties produces a change in the frequency of TCSs, and then based on this phenomenon, we have used a new method of adjusting only the type of edge splicing of the structure to design a novel TCSs combiner that can integrate four TCSs with different frequencies. This work not only expands the variety and number of unexplored TCSs that may exist in a fixed photonic band gap and can be rationalized to be selectively excited in the fixed configuration. Our study provides a feasible pathway for the design of integrated optical devices in which multiple TSs coexist in a single photonic system.

Keywords: valley photonic crystals, topological phase transitions, topological edge states, topological corner states, combiner

PACS: 42.70.Qs, 03.65.Vf, 42.25.Bs, 42.82.Gw

DOI: 10.1088/1674-1056/ada9d9 **CSTR:** 32038.14.CPB.ada9d9

1. Introduction

Inspired by the concept of topological phases in condensed matter physics, topological photonics has been rapidly developed due to its special ability to manipulate light and efficient anti-scattering mechanism.[1–6] In the early days, one of the most classical topological phenomena in topological optical systems was the realization of the TESs by the quantum Hall (QH) effect,[7–9] and the quantum spin Hall (QSH) effect.[10–12] Due to the efficient photon transmission characteristics and anti-scattering robustness of the TESs,[13] they have quite excellent applications in efficient optical transmission behavior.[14–21] Subsequently, the emergence of the quantum valley Hall (QVH) effect,[22–24] which reduced the requirements of the properties of materials and imposed conditions for realizing the topological nontrivial states and enabled more diverse optical field modulations.[25,26] When the all-dielectric VPCs can realize the selective excitation of the TSs by controlling the phase difference of the excitation source, which have become the mainstream object of choice for topological photon transmission.[27–30]

Recent theoretical developments have generalized topological phases to higher orders, higher-order topological insulators (HOTI) have been extensively studied for their unique bulk–edge correspondence principle.[31–33] For example, in a two-dimensional (2D) topological optical system, a 2D topological insulator can have both 1D TESs and 0D TCSs.[34,35] As highly localized cavity modes, the TCSs have the ultra low mode volume as well as the high quality factor,[36–40] which particularly have potential applications in the study of light-matter interactions.[41] A variety of methods for manipulating the TESs have been proposed, however, the research on emerging TCSs is still mainly focused on their complete realization and deeper expansion in properties,[42–46] and how to utilize the proven properties of the TCSs to design novel optical devices will have a broad research outlook. Therefore, we consider the methods of analyzing and manipulating the TESs of VPCs to explore their TCSs, propose a simple method that can integrate different TCSs, and design a novel TCSs combiner.

In this paper, we first theoretically investigate the topological properties of 2D honeycomb VPCs formed by placing two sizes of circular ring dielectric columns in air in the order of honeycomb lattice arrangement. Next, we use the zigzag-type edge (interface I) to connect these two types of VPCs with different topological properties to further explore their TESs, and demonstrate that this structure has efficient photon transmission characteristics and anti-scattering robustness. Moreover, we specifically analyze their TCSs based on the TESs. We first realize the TCSs of the structure, then take the type

†Corresponding author. E-mail: xiaofangxu@aliyun.com

© 2025 Chinese Physical Society and IOP Publishing Ltd. All rights, including for text and data mining, AI training, and similar technologies, are reserved.

of edge splicing as the entry point, and continue to introduce two kinds of bridge-type edges on the basis of the original two kinds of zigzag-type edges. We find that different types of edge splicing produce subtle changes in the frequency of the TCSs, and we explore deeper into this phenomenon and have found a total of four TCSs with different frequencies hidden near the frequencies of 166.8 THz, 169.2 THz, 178.6 THz, and 188.6 THz, which are not only realized in the fixed configuration, but also coexist subtly in the fixed photonic band gap. Finally, based on the above, we design a novel TCSs combiner that can integrate four TCSs with different frequencies, which can selectively excite a single TCSs, thus opening a new way to integrate multiple TCSs in the fixed configuration and photonic band gap. In addition, the material used to design all the structures in this paper is all-dielectric silicon, which is a relatively mature micro-nano material for processing, and the proposed method does not have to change the lattice order, so we believe that this work has potential research value in exploring new applications of integrated photonics.

2. Model and method

The designed VPCs structure is shown in Fig. 1(a), the structure consists of circular ring dielectric columns with ring width ($W = R' - R$) uniformly placed in air with period a (where the outer radius $R' = 100$ nm, the inner radius $R = 50$ nm, and a is the lattice constant, $a = 600$ nm). The region of the regular hexagon is the unit cell of the VPCs, each unit cell contains six identical dielectric columns with C_6 rotational symmetry. And a single honeycomb lattice can also be seen as a composite of two triangular lattices, each containing only A or B type lattice points. In order to make the energy bands of VPCs have different properties at different valleys, it is necessary to break the space inversion symmetry of the structure while keeping the time inversion symmetry unchanged to realize it. As shown in Fig. 1(b), the outer radius R' of all dielectric columns in VPCs remains unchanged, and the inner radius R of the dielectric columns located in the same triangular lattice point sequence are narrowed and expanded respectively ($R_A = 19$ nm and $R_B = 86$ nm) thereby changing the ring width W of dielectric columns. There are two cases, which we define as VPC1 and VPC2.

Since the 2D honeycomb VPCs is periodically arranged in the x–y plane and the dielectric function along the z direction is a constant, these have mirror symmetry in the x–y plane, and thus the eigenmode of the electromagnetic field of the VPCs can be divided into the transverse electric mode (TE mode) and the transverse magnetic mode (TM mode) from the derivation of Maxwell equations.[52] In this paper we consider only the TM mode of electromagnetic wave propagation, i.e., the electric field component propagates along the z direction. The corresponding wave equation to the TM wave is

$$\nabla \frac{1}{\mu(\boldsymbol{r})} \nabla \boldsymbol{E}_z = -\frac{\omega^2}{c^2} \varepsilon_r(\boldsymbol{r}) \boldsymbol{E}_z, \tag{1}$$

where $\varepsilon_r(\boldsymbol{r}) = \varepsilon(\boldsymbol{r})/\varepsilon_0$ is the relative dielectric function, $\mu_r(\boldsymbol{r}) = \mu(\boldsymbol{r})/\mu_0$ is the relative permeability function, $\boldsymbol{E}_z$ is the electric field along the z direction, and c is the velocity of light in air. The solution of this equation satisfies the Bloch theorem when $\varepsilon_r(\boldsymbol{r})$ has periodicity, then we use the finite element simulation software COMSOL to solve the eigenvalue equation and thus obtain the energy bands of VPCs in TM mode.

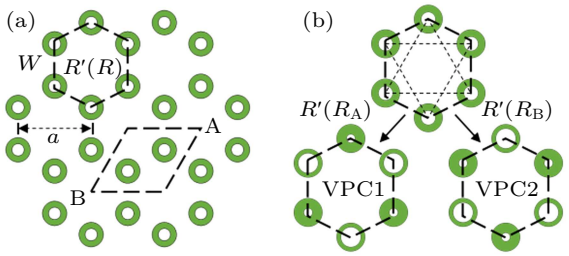


Fig. 1. (a) Schematic diagram of the all-dielectric 2D honeycomb VPCs. (b) Schematic diagram of the unit cells of VPC1 and VPC2.

When the ring width W of dielectric columns is constant, the energy bands of the VPCs is shown in Fig. 2(a), at which time the system is protected by the combined symmetry of time inversion and space inversion, and the first and second energy bands undergo a doubly degenerate at the K (K') point thereby producing a Dirac point with a frequency of 172.26 THz. The illustration shows the first Brillouin zone of the unit cell of the honeycomb lattice, where b_1 and b_2 are the basis vectors of the inverse lattice of the unit cell in reciprocal space, Γ, K, K', and M are higher symmetry points in the first Brillouin zone. The C_6 rotational symmetry of the honeycomb lattice ensures that there always exists a Dirac cone with a linear dispersion relationship near the K (K') point in the first Brillouin zone, which provides a platform for realizing topological valley transmission with the pseudo-spin and energy valleys locked.[53,54]

Next, VPC1 and VPC2 were formed by adjusting the dimensions of the ring width W on the basis of VPCs. Figure 2(b) shows the energy bands of VPC1 or VPC2, and a photonic band gap with a frequency range of 154.41 THz to 219.37 THz was formed between the first and second energy band. At this point the rotational symmetry of the honeycomb lattice is reduced from the original C_6 to C_3, and as a result the degenerate of higher symmetry K (K') point in the first Brillouin is broken, and forming two unequal energy valleys. Photons in different energy valleys will be subjected to effective electromagnetic field of equal intensity and opposite direction, producing the QVH effect. Specifically, photons exhibit singular vortex chirality due to the fact that they carry orbital angular momentum (OAM) with different helical phase

structure. The OAM of light is defined as the helical phase structure of light waves in space, with the numerical value of l, and the different values of l represent different helical phase structures, where l is the orbital quantum number or the topological charge number, whose absolute value and sign represent the helicity and the direction of rotation of the helical phase structure of light waves in space, respectively. Therefore, the following formula can be used to define the helical phase structure of OAM and calculate specific values

$$l = \oint_L \nabla \left[\arg\left(\boldsymbol{E}_z\right)\right] \mathrm{d}\boldsymbol{s}/2\pi, \tag{2}$$

where L is the integral path around the center of the helical phase inspace, and $\nabla\left[\arg\left(\boldsymbol{E}_z\right)\right]$ is the helical phase gradient in space. In Fig. 2(c), the phase change of the first energy band decreases clockwise by 2π at K point and counterclockwise by 2π at K' point. The former light has a right-handed helical phase structure OAM ($l = -1$) near the center of the unit cell, and we define this photonic state as the pseudo-spin-down state in Fig. 2(b); the latter light has a left-handed helical phase structure OAM ($l = -1$) near the center of the unit cell, defining this photonic state as the pseudo-spin-up state.[47] Similarly, the OAM and photonic states of the second energy band at K and K' points are opposite. In addition, VPC2 has the same energy bands as VPC1 due to geometrical equivalence, but these two VPCs exhibit different topological phases, so they cannot be identified simply by the frequency dispersion curve, and it is necessary to introduce the topological invariant to distinguish the topological properties of these two VPCs.

In the presence of time inversion symmetry, the topological invariant describing the topological optical system is defined by the Berry phase of crystals in the k-space:

$$\gamma_n = \oint A_n\left(\boldsymbol{k}\right) \cdot \mathrm{d}\boldsymbol{k}, \tag{3}$$

where the kernel of integral $A_n\left(\boldsymbol{k}\right) = \langle u_{n,\boldsymbol{k}} | \mathrm{i}\nabla \boldsymbol{k} | u_{n,\boldsymbol{k}} \rangle$ is Berry connection, $|u_{n,\boldsymbol{k}}\rangle$ is the periodic Bloch function of the electric field in k-space.[51] In a 2D plane, Berry curvature is

$$\boldsymbol{\Omega}_{\boldsymbol{k}} = \nabla_{\boldsymbol{k}} \times A_n\left(\boldsymbol{k}\right). \tag{4}$$

According to Stokes' theorem, the Chern number for a 2D closed surface is

$$C_n^m = \frac{1}{2\pi} \iint_{\mathrm{BZ}} \Omega_n\left(\boldsymbol{k}\right) \mathrm{d}^2\boldsymbol{k}, \tag{5}$$

thereby the topological invariant can be defined as the valley Chern number, i.e., $C_v^m = C_K^m - C_{K'}^m$, where C_K^m and $C_{K'}^m$ are the Chern numbers corresponding to the centers of the first Brillouin zone taken at K and K' points, respectively, and $m = 1, 2$ denotes VPC1 and VPC2, respectively.[55] Next, we calculated the Berry curvature of the first energy band for VPC1 and VPC2 respectively. As shown in Fig. 2(d), the two have opposite Berry curvature distribution, for VPC1, there are positive (negative) Berry curvature distribution of equal magnitude at the K (K') point, and the valley Chern number $C_v^1 = C_K^1 - C_{K'}^1 = 1/2 - (1/2) = 1$; while for VPC2, there are negative (positive) Berry curvature distribution of equal magnitude at the K (K') point, and the valley Chern number $C_v^2 = C_K^2 - C_{K'}^2 = -1/2 - (1/2) = -1$. Thus, the fact that VPC1 and VPC2 have valley Chern numbers of different signs indicates that each possesses different topological properties.[56]

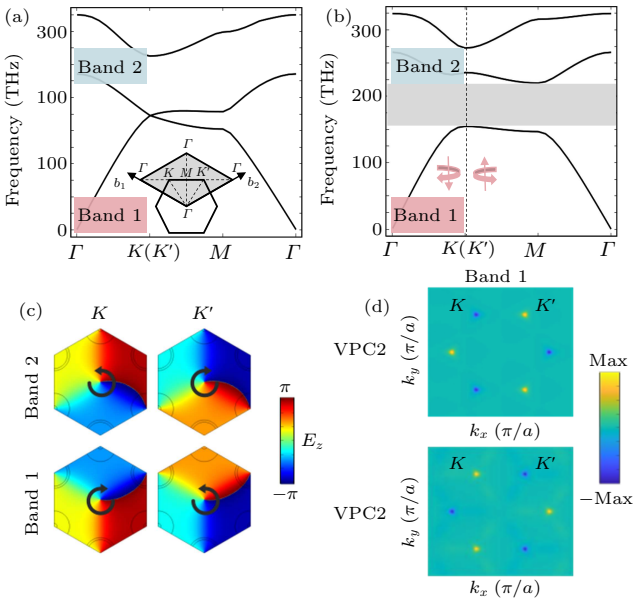


Fig. 2. (a) Photonic energy bands structure of VPCs. (b) Photonic energy bands structure of VPC1 or VPC2. (c) The phase distribution of the E_z (electric field along the z direction) of VPC1 in the first and second energy bands at the K and K' points, respectively. (d) The Berry curvature distribution of VPC1 and VPC2 in the first energy band, respectively.

3. Result and discussion

3.1. Topological transmission

In the previous section we have analyzed that VPC1 and VPC2 possess different topological properties, and according to the bulk–edge correspondence principle, the TESs occur at the edge consisting of two VPCs with a common band gap and different topological phases, which have perfect optical topological properties.

In order to verify the assumption of the existence of the TESs, we drew on previous research,[50] and we splice VPC1 and VPC2 into each other to form the supercell shown in Fig. 3(a), where the type of edge splicing is mainly analyzed as the zigzag-type edge, and due to the difference in the order of the splicing, there are two different zigzag-type edges (interface I and interface II) shown in Figs. 3(b) and 3(c). Then by calculating the dispersion relation of the supercell, two TESs (blue and red) merged together are found to almost run through the entire photonic band gap in Fig. 3(d), where the gray parts are the topological bulk states (TBSs). The slopes

of the curves indicate the propagation directions of the TESs, which have opposite slopes at the K'-valley and K-valley, i.e., the frequency of the pseudo-spin-down state is higher than that of the pseudo-spin-up state at the K'-valley, and the frequency of the pseudo-spin-up state is higher than that of the pseudo-spin-down state at the K-valley. Meanwhile, in order to investigate the properties of the TESs, we choose three points A, B, and C respectively to analyze their E_z intensity distribution. From Fig. 3(e), it can be seen that the electric field of the photonic states at A point is mainly localized at interface I, and the electric field of the photonic states at B and C points is mainly localized at interface II. In both cases the energy is concentrated at the edges of the VPCs of different topological properties, and it rapidly decays along the interior of the crystals from the middle to the two sides, so as to realize the localization of the optical field. Then, by analyzing the Poynting vector distribution of the energy at B and C points in Fig. 3(f), it is found that the pseudo-spin-down states of the K'-valley are transmitted only along the Γ–K' direction, i.e., to the left; while the pseudo-spin-up states of the K-valley are transmitted only along the Γ–K direction, i.e., to the right. The different pseudo-spin states of the two energy valleys are transmitted along different directions, thus realizing the selective coupling and transmission of the pseudo-spin and energy valleys locked, i.e., the K'-valley and K-valley are selective for left-handed circularly polarized (LCP) light and right-handed circularly polarized (RCP) light, respectively.

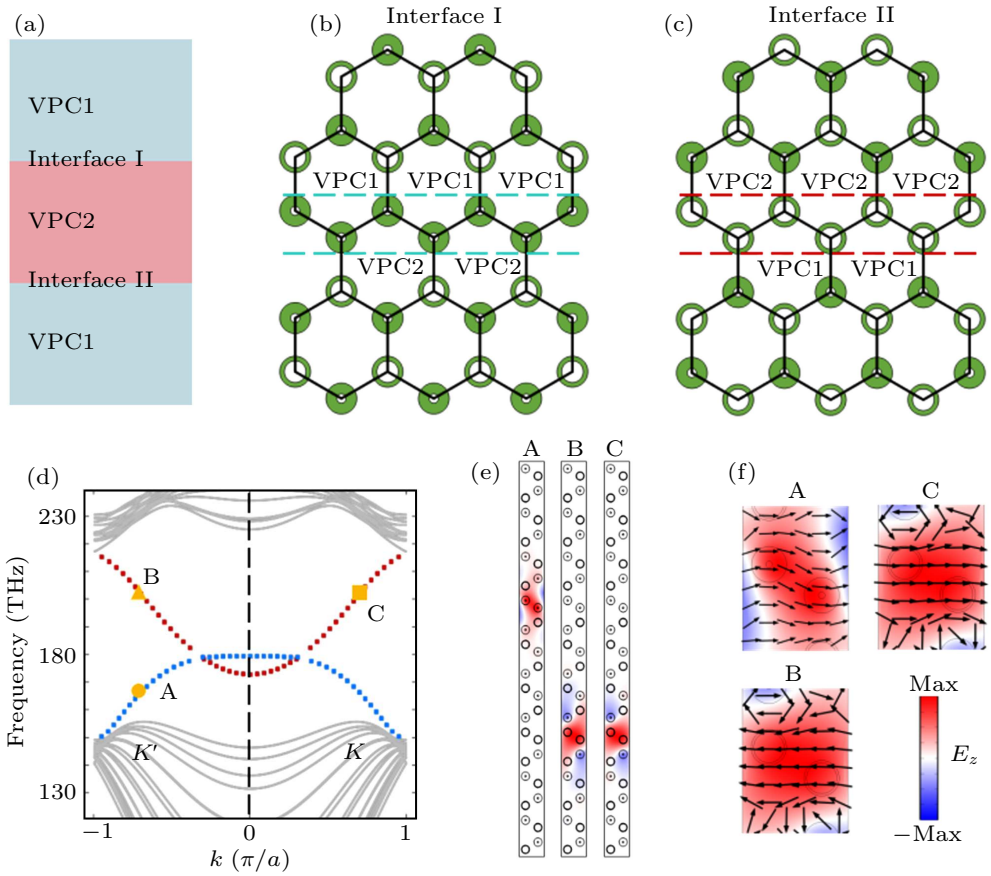


Fig. 3. (a) Schematic diagram of the supercell with both interface I and interface II constructed by VPC1 and VPC2. (b) and (c) The arrangement of the supercells for interface I and interface II. (d) Photonic energy bands structure of the constructed supercell, the blue and red dots indicate two kinds of TESs. (e) The E_z intensity distribution obtained by taking A, B, and C points in the two TESs, respectively. (f) The Poynting vector distribution of the energy at A, B, and C points, respectively.

In order to show more intuitively that this structure has efficient photon transmission characteristics and anti-scattering robustness, we constructed the straight waveguide, the Z waveguide, and the Z-defect waveguide formed by introducing four defects at the same time, and placed four point light sources at the edge between VPC1 and VPC2, which are uniformly distributed on a circle with a radius of $0.03a$, and by controlling the phase difference between them we can form LCP or RCP light to be used as the excitation source of the electric field, respectively. Figure 4(a) shows the constructed straight waveguide structure; figure 4(b) shows the E_z intensity distribution of the straight waveguide when the frequency of the excitation source is taken to be 156.9 THz (all the following), in which the yellow pentagram denotes the position of the excitation source (RCP), and it can be seen that light is transmitted along the edge to the right, which has a stable anti-scattering property; figures 4(c) and 4(d) show the E_z intensity distribution corresponding to the positions of the

excitation sources (LCP and RCP) taken at the center of the edge, respectively, where LCP light is transmitted along the left and RCP light is transmitted along the right, thus exhibiting a good unidirectional transmission property. In addition, when light is transmitted in traditional micro-nano optical devices, it is inevitable to encounter interference effects such as sharp turns, defects, etc., which will reduce the transmission efficiency of light in optical devices, and topological optical devices are more robust to the above problems. For example, figure 4(e) shows the constructed Z waveguide structure with 60° sharp bends, and the E_z intensity distribution of the Z waveguide shown in Fig. 4(f) fully proves the anti-interference property of the structure in the face of sharp turns. As shown in Fig. 4(g), we also introduce defects such as cavity, misalignment, disorder, and impurity into the transmission path of the Z waveguide in turn, and figure 4(h) demonstrates that the structure is still able to maintain a stable transmission property. Finally, we place edge-probes at the input and output ports of each of the three waveguides and calculate the transmission efficiency of each waveguide by simulating the average surface density of the time-averaged power outflow of the measured energy, and the transmission efficiency of the waveguide can be defined as

$$T = \frac{P_{\text{out}}}{P_{\text{in}}} = \frac{\iint P_{\text{out}}\,\mathrm{d}s}{\iint P_{\text{in}}\,\mathrm{d}s}, \tag{6}$$

where P_{in} and P_{out} are the total power at the input and output ports, respectively. From Fig. 4(i), it can be seen that the transmission efficiency of all three waveguides can reach more than 99% in the frequency range of 155 THz–173 THz, which has a strong transmission property.

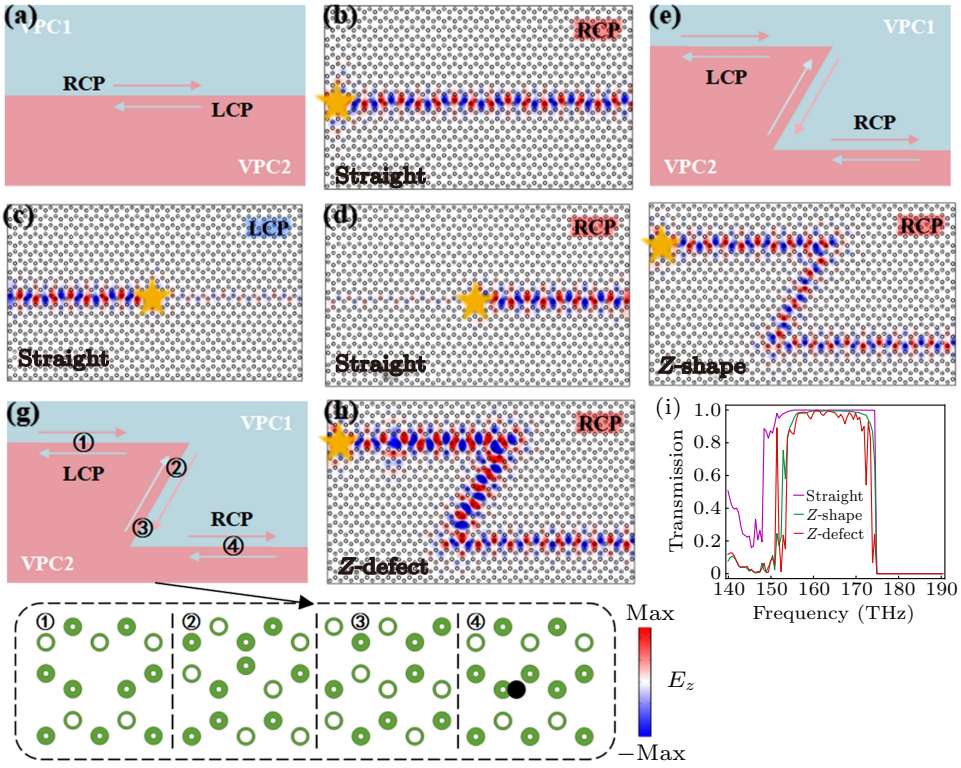


Fig. 4. (a) The straight waveguide structure. (b) The E_z intensity distribution of the straight waveguide when the excitation source (RCP) is placed on the left side. (c) and (d) The E_z intensity distribution of the straight waveguide when the excitation (LCP and RCP) source is placed in the middle, respectively. (e) The Z waveguide structure with 60° sharp bends. (f) The E_z intensity distribution of the Z waveguide. (g) The upper part shows the locations where defects such as cavity, misalignment, disorder, and impurity are sequentially introduced into the Z waveguide structure, and the lower part shows the supercells at the corresponding locations after the introduction of the defects. (h) The E_z intensity distribution of the Z-defect waveguide. (i) Calculated transmission efficiency curve include the straight waveguide, Z waveguide, and Z-defect waveguide.

3.2. Topological corner states combiner

In recent years, a number of novel optical phenomena and properties have been discovered with the introduction of the concept of higher-order topology and the existence of topological invariant and corresponding symmetries. For example, HOTI support not only 1D TESs, but also 0D TCSs. By analogy with related studies of the TESs, we find that different types of edge splicing have a slight effect on the frequency of the TCSs.

Firstly, in order to better observe the TCSs, we constructed a two-layer equilateral triangular supercell. As shown in Fig. 5(a), this structure is composed of 45 VPC1 surrounded by 145 VPC2, with the inner edge length of 10a and the outer edge length of 20a. The reason for designing it into this shape is that the formation of the TCSs has a selective law on the internal angles of the structure, which can be interpreted as a

result of the valley–valley interactions.[48] And this structure contains 3 internal 60° angles, each of which can form the TCSs, which is the theoretical basis for the shape design of all the following structures in this paper. At the same time, we adopt the types of splicing of all the three internal edges as the interface I in Fig. 3(b), and apply the perfect electric conductor (PEC) boundary condition to the outermost part of the structure, and we will refer to this structure as the T–I-type structure for short in the following. Figure 5(b) shows the calculated discrete characteristic frequencies of the T–I-type structure, where the TESs (blue dots) and the TCSs (red dots) exist between the photonic band gap of the entire TBSs (gray dots), and the upper TBSs appear outside the range of coordinates of the given frequencies and the TCSs exist in isolation, which can be understood in conjunction with Fig. 3(d). In addition, the three C_1-type TCSs are labeled with C_{11}, C_{12}, and C_{13}, respectively. Figure 5(c) demonstrates the frequencies and E_z intensity distributions of the three C_1-type TCSs, each of which has the electric field that is only highly localized among the sublattice at the corner and exhibits an exponential decay along the region away from the corner. Note that the frequencies of the three TCSs are not perfectly simple and there is a small frequency difference due to the effect of mutual interference of the space electric field of the three TCSs in the tight-binding model. Nevertheless, the excellent corner localization property, which is significantly different from that of the TESs, is also well demonstrated.

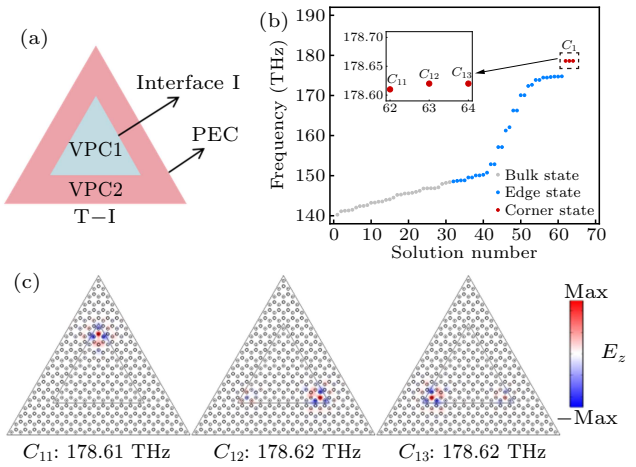


Fig. 5. (a) Schematic diagram of the T–I-type structure. (b) Calculated discrete characteristic frequencies of the T–I-type structure. (c) The frequencies and E_z intensity distributions of the three C_1-type TCSs.

Then we consider the types of splicing of the internal edges of the structure to be all of the interface II in Fig. 3(b), and the external conditions remain unchanged. Due to the unique arrangement of the honeycomb lattice, at this point it is necessary to exchange the positions and numbers of VPC1 and VPC2 in the T–II-type structure to construct the T–II-type structure as shown in Fig. 6(a). Figure 6(b) shows the calculated discrete characteristic frequencies of the T–II-type structure, and the three C_2-type TCSs are labeled with C_{21}, C_{22}, and C_{23}, respectively. Figure 6(c) similarly demonstrates the frequencies and E_z intensity distribution of the three C_2-type TCSs. It can be seen that the C_2-type TCSs still exist in isolation, but there is a significant change in the frequency compared to the C_1-type TCSs. In our previous research on the TCSs, we found that although there are different principles for the generation of the TCSs, all the TCSs appear in the photonic band gap of the whole TBSs, so we can generalize that changing the type of edge splicing of the structure not only changes the frequency range of the TESs,[49] but also changes the frequency of the TCSs slightly.

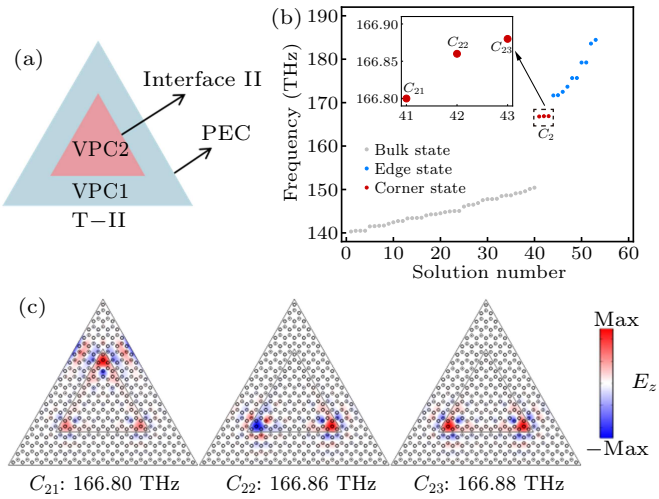


Fig. 6. (a) Schematic diagram of the T–II-type structure. (b) Calculated discrete characteristic frequencies of the T–II-type structure. (c) The frequencies and E_z intensity distributions of the three C_2-type TCSs.

Next, we introduce another common type of edge splicing (Bridge-type edge) to explore more about the effect of different types of edge splicing on the frequency of the TCSs as a way to obtain the TCSs with different frequencies that may exist in the same photonic band gap of the VPCs. Similarly, due to the different splicing order, there will exist two different Bridge-type edges, interface III and interface IV, as shown in Figs. 7(a) and 7(b). Figures 7(c) and 7(d), on the other hand, are based on the T–I-type structure and the T–II-type structure, respectively, and only the types of splicing of their internal edges are all replaced with the interface III and interface IV, resulting in the T–III-type structure and the T–IV-type structure. Figures 7(e) and 7(f) correspond to the calculated discrete characteristic frequencies, respective, and the three C_3-type TCSs are labeled with C_{31}, C_{32}, and C_{33}, and the three C_4-type TCSs are labeled with C_{41}, C_{42}, and C_{43}, respectively. Figures 7(g) and 7(h) show the frequencies and E_z

intensity distribution of the three C_3-type TCSs and three C_4-type TCSs, respectively. From the above results, it can be seen that by replacing them again with other types of edge splicing, the frequencies of the TCSs will still have their own completely different variations, which further confirms our idea.

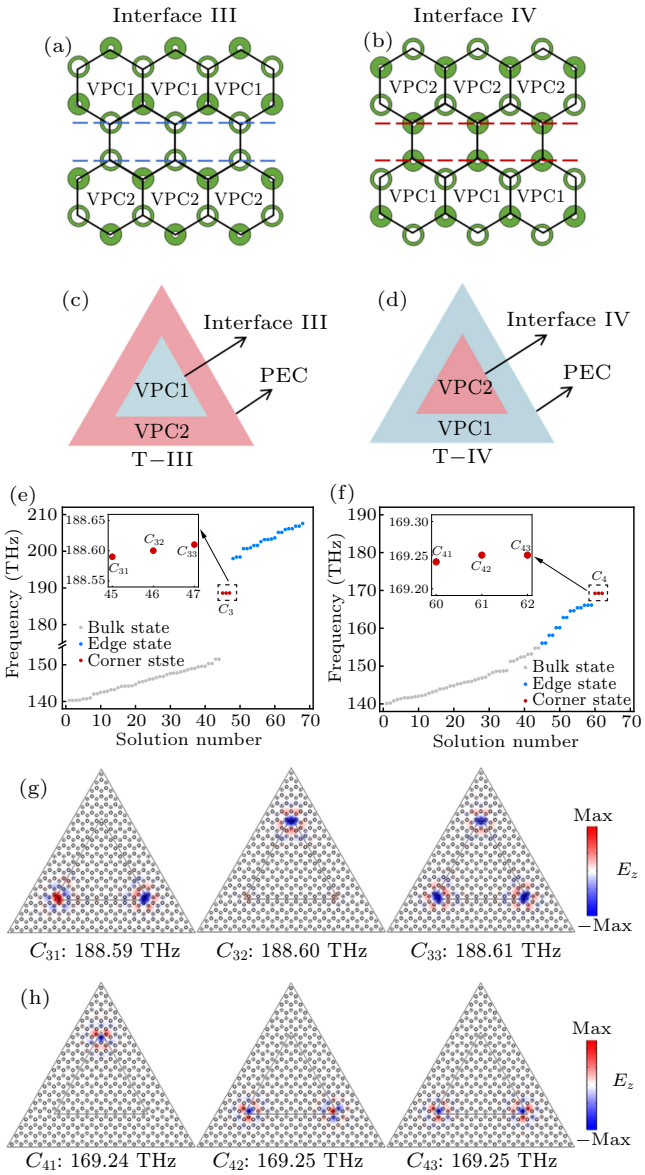


Fig. 7. (a) and (b) The arrangement of the supercells for interface III and interface IV. (c) and (d) Schematic diagram of the T–III-type and T–IV-type structures. (e) and (f) Calculated discrete characteristic frequencies of the T–III-type and T–IV-type structures. (g) and (h) The frequencies and E_z intensity distributions of the three C_3-type and the three C_4-type TCSs.

In addition to investigating the effects of different types of edge splicing on the TCSs, we also considered whether the above four types of edge can exist simultaneously in the system, which in turn can realize the idea of integrating multiple TCSs in the fixed configuration and the fixed photonic band gap. The novel TCSs combiner named funnel-type structure that we designed to integrate the above four TCSs with different frequencies is shown in Fig. 8(a), in which the four edges are connected into a funnel-type path by forming a 60° angle inside the structure, respectively; figure 8(b) is the calculated discrete characteristic frequencies of the funnel-type structure; figure 8(c) shows the single C_1-type, C_2-type, C_3-type, and C_4-type TCSs, which can be selectively and singly excited in the corresponding internal corner region of the funnel-type path; figure 8(d) shows the E_z intensity and frequency dependence curve measured by placing a corner-probe at each internal corner, which shows that each TCSs has the unique high-intensity electric field at the corresponding frequency, and the other parts of the structure are affected by the TESs or TBSs to produce the low-intensity electric field, and the contrast between the two demonstrates the excellent and selectable corner localization property.

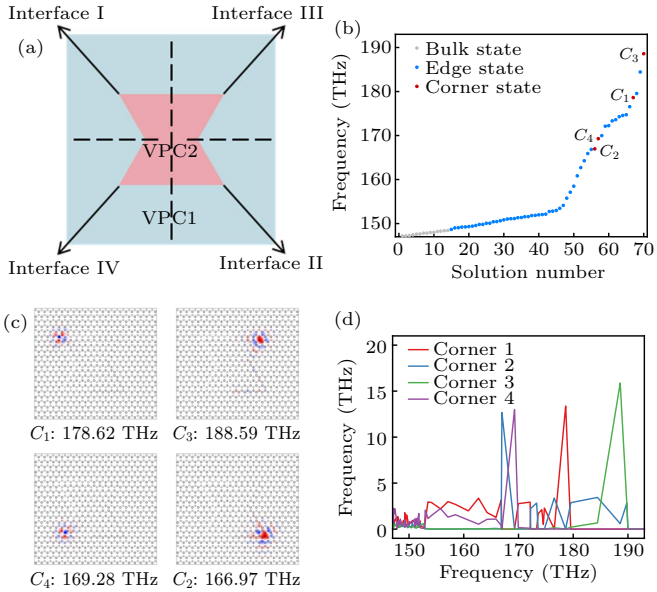


Fig. 8. (a) Schematic diagram of the TCSs combiner named funnel-type structure. (b) Calculated discrete characteristic frequencies of the funnel-type structure. (c) the frequencies and E_z intensity distributions of the single C_1-type, C_2-type, C_3-type, and C_4-type TCSs. (d) Calculated E_z intensity and frequency dependence curve.

4. Conclusion

In summary, we theoretically realized the TSs of VPCs composed of circular ring dielectric columns in the order of honeycomb lattice arrangement. Specifically, we demonstrated that the TESs of this structure have efficient photon transmission characteristics and anti-scattering robustness, found that different types of edge splicing produce subtle changes in the frequency of the TCSs, and then based on this phenomenon designed a novel TCSs combiner that can integrate multiple TCSs in a fixed photonic band gap and the fixed configuration by using a new method of adjusting the type of edge splicing only. Our research content makes the manipulation of TCSs more diversified, and at the same time may provide new possibilities for the design and application of novel topological optical devices in the current domain of micro-nano integrated photonics.

References

[1] Wang Z, Chong Y D, Joannopoulos D and Soljačić M 2009 *Nature* **461** 772
[2] Hafezi M, Mittal S, Fan J, Migdall A and Taylor J M 2013 *Nat. Photon.* **7** 1001
[3] Bansil A, Lin H and Das T 2016 *Rev. Mod. Phys.* **88** 021004
[4] Qi X L and Zhang S C 2011 *Rev. Mod. Phys.* **83** 1057
[5] Khanikaev A B and Shvets G 2017 *Nat. Photon.* **11** 763
[6] Ozawa T, Price H M, Amo A, Goldman N, Hafezi M, Lu L, Rechtsman M C, Schuster D, Simon J, Zilberberg O and Carusotto I 2019 *Rev. Mod. Phys.* **91** 015006
[7] Haldane F D M and Raghu S 2008 *Phys. Rev. Lett.* **100** 013904
[8] Fang K J, Yu Z F and Fan S H 2012 *Nat. Photon.* **6** 782
[9] Wang M D, Zhang R Y, Zhang L, Wang D Y, Guo Q H, Zhang Z Q and Chan C T 2021 *Phys. Rev. Lett.* **126** 067401
[10] Wu L H and Hu X 2015 *Phys. Rev. Lett.* **114** 223901
[11] Barik S, Karasahin A, Flower C, Cai T, Miyake H, DeGottardi W, Hafezi M and Waks E 2018 *Science* **359** 666
[12] Yang Z Q, Shao Z K, Chen H Z, Mao X R and Ma R M 2020 *Phys. Rev. Lett.* **125** 013903
[13] Hasan M Z and Kane C L 2010 *Rev. Mod. Phys.* **82** 3045
[14] Liang G Q and Chong Y D 2013 *Phys. Rev. Lett.* **110** 203904
[15] Chen M L, Jiang L J, Lan Z H and Sha W 2020 *IEEE Trans. Antennas Propag.* **68** 609
[16] Yang Y T, Qian X Y, Shi L W, Shen X P, Wang Y F and Hong H 2022 *Opt. Express* **30** 5731
[17] Yuan M, Xu T and Hang Z 2021 *Light Sci. Appl.* **9** 127
[18] Ruan Y H, Qian X Y, Wang H X, Hu Z D, Yang Y T, Wang J C, Shen X P and Wang Y F 2023 *Photon. Res.* **11** 569
[19] Zhang Y Q, Kartashov Y V, Zhang Y P, Torner L and Skryabin D V 2018 *Laser Photon. Rev.* **12** 1700348
[20] Chen J, Liang W and Li Z Y 2020 *Opt. Lett.* **45** 4964
[21] Liu J W, Shi F L, Shen K, Chen X D, Chen K, Chen W J and Dong J W 2023 *Nat. Commun.* **14** 2027
[22] Wu X X, Meng Y, Tian J X, Huang Y Z, Xiang H, Han D Z and Wen W J 2017 *Nat. Commun.* **8** 1304
[23] Noh J, Huang S, Chen K P and Rechtsman M C 2018 *Phys. Rev. Lett.* **120** 063902
[24] Gao F, Xue H R, Yang Z J, Lai K F, Yu Y, Lin X, Chong Y D, Shvets G and Zhang B L 2018 *Nat. Phys.* **14** 140
[25] Schaibley J R, Yu H, Clark G, Rivera P, Ross J S, Seyler K L, Yao W and Xu X 2016 *Nat. Rev. Mater.* **1** 16055
[26] Chen Y, He X T, Cheng Y J, Qiu H Y, Feng L T, Zhang M, Dai D X, Guo G C, Dong J W and Ren X F 2021 *Phys. Rev. Lett.* **126** 230503
[27] Chen X D, Zhao F L, Chen M and Dong J W 2017 *Phys. Rev. B* **96** 020202
[28] He X T, Guo C H, Tang G J, Li M Y, Chen X D and Dong J W 2022 *Phys. Rev. Appl.* **18** 044080
[29] Lévêque G, Pennec Y, Szriftgiser P, Amo A and Martínez A 2023 *Phys. Rev. Appl.* **108** 043505
[30] Han J F, Liang F, Zhao Y L, Lui J L, Wang S C, Wang X R, Zhao D S and Wang B Z 2024 *Phys. Rev. Appl.* **21** 014046
[31] Xie B, Wang H X, Zhang X, Zhan P, Jiang J H, Lu M and Chen Y 2021 *Nat. Rev. Phys.* **3** 520
[32] Zhou R, Lin H, Wu Y J, Li Z F, Yu Z H, Liu Y and Xu D H 2022 *Photon. Res.* **10** 1244
[33] Jia S Y, Huang R W, Hu J Z, Jiang Y, Huang H, Xie B Y, Lu M H, Zhan P, Chen Y F and Wang Z L 2023 *Laser Photon. Rev.* **17** 2200949
[34] Kim M and Rho J 2020 *Nanophotonics* **9** 3227
[35] Chen Y F, Lan Z H, Zhu J and Su Z Q 2023 *Opt. Laser Technol.* **158** 108865
[36] Ota Y, Liu F, Katsumi R, Watanabe K, Wakabayashi K, Arakawa Y and Iwamoto S 2019 *Optica* **6** 786
[37] Luo X W and Zhang C W 2019 *Phys. Rev. Lett.* **123** 073601
[38] He X T, Li M Y, Qiu H Y, Ruan W S, Zhou L D, Liu L, Chen X D, Chen W J, Zhao F L and Dong J W 2021 *Photon. Res.* **9** 1423
[39] Wu S Q, Jiang B, Liu Y and Jiang J H 2021 *Photon. Res.* **9** 668
[40] Zhang Z J, Yang J B, Du T and Jiang X P 2022 *Photon. Res.* **10** 855
[41] Rao M J, Shi F L, Rao Z X, Yang J W, Song C K, Chen X D, Dong J W, Yu Y and Yu S Y 2024 *Light: Sci. Appl.* **13** 19
[42] Peng Y C, Liu E X, Yan B, Xie J L, Shi A Q, Peng P, Li H and Liu J J 2022 *Opt. Lett.* **47** 3011
[43] Li M X, Wang Y K, Sang T, Chu H C, Lai Y and Yang G F 2022 *Photon. Res.* **10** 197
[44] Wei M S, Liao M J, Wang C, Zhu C J, Yang Y P and Xu J P 2023 *Opt. Express* **31** 3427
[45] Hu T Y, Zhong W L, Zhang T F, Wang W H and Wang Z F 2023 *Nat. Commun.* **14** 7092
[46] Wang C T, Liu F and Huang H Q 2022 *Phys. Rev. Lett.* **129** 056403
[47] Yang Y T, Jiang H and Hang Z H 2018 *Sci. Rep.* **8** 1588
[48] Phan H T, Liu F and Wakabayashi K 2021 *Opt. Express* **29** 18277
[49] Bakhtiyar O and Romain F 2019 *Nanophotonics* **8** 1433
[50] Zhong H, Kartashov Y V, Zhang Y Q, Song D H, Zhang Y P, Li F L and Chen Z G 2019 *Opt. Lett.* **44** 3342
[51] Zhong H, Wang R, Belić M R, Zhang Y P and Zhang Y Q 2019 *Opt. Express* **27** 6300
[52] Tang Q, Belić M R, Zhong H, Cao M, Li Y D and Zhang Y Q 2024 *Opt. Lett.* **49** 4110
[53] Guo W X and Liu W M 2022 *Chin. Phys. B* **31** 057302
[54] Wang X R, Fei H M, Lin H, Wu M, Kang L J, Zhang M D, Liu X, Yang Y B and Xiao L T 2023 *Chin. Phys. B* **32** 074205
[55] Wang Q and Hao N 2024 *Chin. Phys. B* **33** 127303
[56] Chen S H, Qi Y, Li Y C, Wang Q H and Xiang X J 2024 *Chin. Phys. B* **33** 118701